A COMPUTATIONAL STUDY OF BURNER FAILURE RELATED LOW ENGINE ORDER FORCED RESPONSE MECHANISMS IN A HIGH PRESSURE TURBINE

Alexander Trafford
Vibration UTC,
Dept. of Mechanical Engineering,
Imperial College London,
London SW7 2AZ, UK
Email: a.trafford20@imperial.ac.uk

Dr Sina Stapelfeldt
Vibration UTC,
Dept. of Mechanical Engineering,
Imperial College London,
London SW7 2AZ, UK
Email: s.stapelfeldt@imperial.ac.uk

Dr Ricardo Puente
Vibration UTC,
Dept. of Mechanical Engineering,
Imperial College London,
London SW7 2AZ, UK
Email: r.puente@imperial.ac.uk

ABSTRACT

This paper carries out a computational study of the effect of temperature distortions, representative of the presence (or lack thereof) of upstream burner can distortions, on the Low Engine Order (LEO) forced response mechanisms in a High Pressure Turbine (HPT). This type of forced response occurs at frequencies below the Stator Blade Passing Frequency (SBPF) and can be highly damaging for turbines due to their tendency to excite fundamental modes of vibration at engine operating speeds. With transitions in the aerospace industry toward using alternative fuels likely to affect the nature of combustor distortions impinging on the HPT and a push toward low NOx combustion increasing the likelihood of burner valve failure, the importance of burner distortions on turbine forcing is rising. This paper investigates the mechanisms through which burner can hot-streaks force vibration in turbines, by examining their effect on rotor blade unsteady pressure. Comparisons are made between the hot-streaks and two burner failure cases, a 1 burner failed event and a symmetric 2 burner failed event, with results showing variation in the severity of different forcing mechanisms between hot-streak and cold-streak forcing. This information will be crucial for developing both life prediction methods as well as early-stage design tools with the aim of forcing attenuation.

KEYWORDS High Pressure Turbine, Low Engine Order, Forced Response, Blocked Burner, Aeroelasticity

NOMENCLATURE

$()_{h/c}$	Quantity measured at the hub/ casing
$()_\theta$	Refers to the circumferential direction
$()_{1/3}$	Refers to the turbine inlet/outlet
$()_2$	Refers to the vane exit
$()_r$	Refers to the radial direction
$()_x$	Refers to the axial direction
$\overline{()}$	Time averaged quantity
$()_{rel}$	Relative quantity
$()_0$	Total quantity
A	Area, m^2
b_h	Blade height
ρ	Density, kgs^{-1}
M	Mach number
p	Pressure, Pa
N	Set of all burners around annulus, $1-16$
ψ	Stage loading coefficient, $\frac{\Delta h_0}{U^2}$
T	Temperature, K
t	Time in seconds, s
Y_p	Turbine total pressure loss coefficient, $\frac{P_{03}-P_3}{P_{01}-P_{03}}$
c	Velocity, ms^{-1}
CFD	Computational Fluid Dynamics
EO	Engine Order
HEO	High Engine Order
HPT	High Pressure Turbine
LEO	Low Engine Order
SBP	Stator Blade Passing

1 INTRODUCTION

The future of both conventional fuel and Sustainable Aviation Fuel (SAF) burning turbofan aeroengines will rely on lean burn combustors for reducing NOx. One unfortunate side effect of this technology is the increased likelihood of burner valve failure, an event that can be a driver of Low Engine Order (LEO) forced vibration. This type of forced response occurs at frequencies below the blade passing frequency, and can be highly damaging for turbines due to their tendency to excite low frequency fundamental modes of vibration at engine operating speeds.

Early attempts to simulate LEO forcing computationally investigated aeromechanical mistuning in vane stagger [1] [2]. However, due to the high computational cost of running full annulus calculations, these studies were run inviscidly; a potentially prohibitive weakness for temperature distortion driven LEO forcing considering the long standing knowledge that temperature variations across an annulus can interact with secondary flows in the rotor [3] [4]. Attempts to investigate reduced domain models have had limited success [5], with Elliot et al [6] showing reasonable experimental agreement for well-defined LEO aeromechanical mistuning. However, drivers of LEO vibration rarely tend to be intentionally included in turbine geometries and in comparison to HEO equivalents, such as vane count, are often not known in advance of manufacture.

In the case of inlet temperature distortions, another difficulty arises due to their tendency to persist throughout all stages of turbines [7][8][9][10]. Mayorca et al [9] found that burner can induced forcing is most severe for the final blade row and is more significant than SBPF forcing. The importance of considering multiple rows in LEO forcing calculations has been shown by Fridh et al's study looking at the influence of partial admission on LEO forcing in a two stage industrial test turbine rig [11] and through the LEO Tyler-Sofrin modes [12] reported in [13].

Breard et al's [14] parametric study includes the first attempt to quantify the effect of burner can failure on HPT forcing and unveiled LEO forcing's apparent dependence on complex geometrical features and their phases. Khafedzhiyski et al [15] is the only other work to investigate something similar; in this case different configurations for burner can staging (equivalent in practice to burner can failure) in order to reduce the forcing seen at specific EOs of interest. Results showed that EOs of relevance could be reduced for all turbine rows, but at the cost of additional EOs excitations not previously observed.

All of this pushes computational models looking to capture LEO forcing toward being high-fidelity, full annulus, multi-row simulations that are not possible until very late stages of the design process, where the forcing sources themselves are often frozen into the design of the turbine. Yet as temperatures in turbines continue to rise, in response to the demand for greater and greater efficiencies, the necessity of computational tools for forcing predictions that circumvent expensive and potentially unfeasible strain gauge testing has never been more pressing. Any tool that could be useful in design for LEO forcing attenuation will need to be based on the foundation of a strong understanding of the physical mechanisms that underpin LEO forcing in turbines.

This paper carries out a study of the effect of inlet total temperature distortions, representative of the presence (or lack thereof) of upstream burner-can hot-streaks, on the LEO forced response of a High Pressure Turbine (HPT) rotor. In response to research indicating the importance of distortion shape [14] [9] [16], extensive effort has been put into creating detailed and accurate inlet temperature distortions, beyond the scope of any previous work in this area. Unsteady lift forces and pressure magnitudes on the rotor blade of a HPT turbine rig stage are compared with the aim of determining:

1. Which aerodynamic features of hot-streaks drive LEO forcing, and through which mechanisms does this forcing act
2. How severe are burner failures, as drivers of LEO forced response, and how do the mechanisms of burner failure forcing differ from that of hot-streaks

It is believed that through detailed analysis of the forcing mechanisms triggered by burner can failure, information crucial for both life prediction as well as early stage design methods, with the goal of forcing attenuation, will be uncovered.

2 METHODOLOGY

2.1 MT1 Turbine Stage

This study is carried out by imposing temperature distortions as inlet boundary conditions to unsteady simulations of the MT1 HPT rig. The MT1 stage is a low temperature, unshrouded, HP turbine, with 32 vanes and 60 rotor blades onto which a hypothetical 16 burner arrangement has been imposed. A representation of the turbine geometry can be seen in Figure 1. This stage has been tested extensively at the QinetiQ Turbine Test Facility, which is a short duration light piston turbine rig, designed for heat transfer experiments across a 500ms steady state operating window. The rig steady operating point used for this study is that for the uncooled configuration and further description of this rig can be found in [17].

2.2 Numerical solver and Set-up

This research has been carried out entirely computationally, using the in-house aeroelasticity solver AU3D [18]. AU3D is a non-linear aeroelasticity tool, that uses a Favre-Averaged Navier-Stokes CFD solver. The discretisation is 2nd order accurate in space [19] with fully implicit 2nd order accurate dual time stepping. This work uses a variant of the Spallart-Almaras turbulence model, with wall functions, where the turbulence production term is corrected using pressure gradient and helicity [20].

The simulations are run as full annulus unsteady calculations using the converged steady state solution as a starting point (unless the nature of the distortion allows for taking advantage of sectorial periodicity). As a result of a time step convergence study, the simulations use 160 time steps per rotor blade passing (300

per SBP) and the unsteady pressures on the blade surface are sampled every two time steps. The mesh for this study is a structured mesh built using the software PADRAM [21], for which the radial layer count and vane wake definition were determined through a mesh independence study, with the aim of reducing density without an excessive cell expansion ratio or vane trailing edge skewness. The total cell count is such that the full annulus mesh has approximately 115 million nodes, with a y+ value of 40. The interface between the stator and rotor domains is modelled as a sliding plane, for the unsteady calculation and a mixing plane for the initial steady-state runs. A representation of the mesh at the vane trailing edge, rotor leading edge and across the sliding plane can be seen in Fig 1.

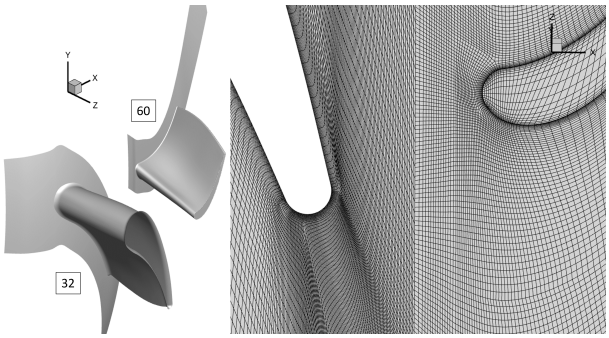

FIGURE 1. MT1 STAGE DOMAIN WITH VANE/BLADE COUNTS (LEFT) & MESH ACROSS SLIDING PLANE AT CASING (RIGHT)

2.3 Boundary Condition Parameterisation

The inlet distortions are constructed in order to accurately recreate the time averaged static temperature field obtained from a high fidelity CFD simulation at the combustor exit of a large civil aeroengine. These distortions show no relation between any other key flow property and the static temperature distortion, a finding echoed by [22], so in this work burner failure is treated as a purely temperature based phenomenon. The temperatures, as they are seen from the combustor exit, are scaled down to match the area-averaged mean temperature of the MT1 rig.

Due to the need to study burners that are inactive, a process of parameterisation is undertaken to create a distortion that is as accurate as possible in a physical sense to the original scaled distortion, but that is constructed as a superposition of 16 discrete temperature source terms, each representing one burner. The equation for the inlet temperature distortions takes the form of that shown in Eqn (1), and has an RMS error of 1.69% compared with the original scaled distortion for the all-burners active case. Eqn 1 takes this form in order to allow for highly accurate capture of the distortion spatial harmonic content. It consists of two terms which in turn govern the mean/1st harmonic contribution of each active burner (T_1, Eqn (2)) and the 2nd harmonic contribution (T_2, Eqn (3)) of the parameterised temperature distortion.

$$T(r,\theta) = \Sigma_{i=[]}^{N} A_1(r) N_\theta(\mu_i(r), \sigma_1(r)^2) + \Sigma_{i=[]}^{N} \Lambda(\mu_i, \frac{\pi}{8}) \left\{ \Sigma_{j=1}^{j=32} A_2(r) N_\theta(\mu_j(r), \sigma_2(r)^2) - \overline{\Sigma_{j=1}^{j=32} A_2(r) N_\theta(\mu_j(r), \sigma_2(r)^2)} \right\} + T_{back}(r) \quad (1)$$

For the 0th harmonic (mean) and 1st harmonic component, the temperature sources are modelled as Gaussian functions [23] $N_\theta(\mu_i(r), \sigma_1(r)^2)$, multiplied by a scaling factor $A(r)$, atop a background static temperature varying from hub to tip $T_{back}(r)$. Both the scaling factor and the variance of the normal distribution vary as functions of radial position. These are tuned such that the resulting 2D temperature field (Eqn (2)) is an exact recreation of the mean of the original scaled distortion and is accurate for the first harmonic magnitude to within $0.5K$ at all radii except for $\leq 0.02 b_h$ and $> 0.99 b_h$, at which points boundary layer effects are the pre-dominant driver of the distortion strength. With the normal distribution used in this way, the mean component $\mu_i(r)$ corresponds to the circumferential centre of the temperature hot-streak seen due to the burner i, whilst $\sigma_1(r)$ determines the spread of the hot-streak in the θ direction. In general, the burner hot-streaks are clocked such that each value $\mu_i(r)$ is located at $\theta = \frac{(i-1)2\pi}{16}$ radians and impinge on one in every two stator vanes. However, the values of $\mu_i(r)$ vary slightly with radial position, in order to capture the circumferential 'phase' of the temperature distortions over the portion of the radius for which the hot-streak is centred (namely from about $60-95\% b_h$). $i = []$ is a subset of all active burners, from the complete burner set N, given in Table 2.4 for each case run.

$$T_1(r,\theta) = \Sigma_{i=[]}^{N} A_1(r) N_\theta(\mu_i(r), \sigma_1(r)^2) + T_{back}(r) \quad (2)$$

$$T_2(r,\theta) = \Sigma_{i=[]}^{N} \Lambda(\mu_i, \frac{\pi}{8}) \left\{ \Sigma_{j=1}^{j=32} A_2(r) N_\theta(\mu_j(r), \sigma_2(r)^2) - \overline{\Sigma_{j=1}^{j=32} A_2(r) N_\theta(\mu_j(r), \sigma_2(r)^2)} \right\} \quad (3)$$

A summation of equispaced normal distributions like this, produces an almost sinusoidal wave at each radius, with negligible higher harmonic components. This work captures the variation in the second harmonic of the original temperature distortion by adding a second wave with twice the frequency (given in Eqn 3) atop that given for each radius in Eqn 2. The second harmonic component of the temperature distortion is plagued by the added complication of relating a 32EO temperature variation to a set of 16EO discrete burners. The approach taken here is that the magnitude of the underlying 32EO variation is captured by a similar

process to that used for the 1st harmonic, only with the mean removed. This is then multiplied by a separate wave, constructed as a superposition of impact-area pulses: one for each active burner.

$$\Lambda(\mu_i, \frac{\pi}{8}) = \begin{cases} \frac{1}{2} + \Sigma_{n=1}^{9} 2\frac{1-(-1)^n}{(\pi n)^2} cos(16n\theta + \mu_i), \\ \qquad\qquad \mu_i - \frac{\pi}{16} \leq \theta < \mu_i + \frac{\pi}{16} \\ 0, \qquad\qquad elsewise \end{cases}$$

In this work, the area of impact for each discrete burner is modelled as a triangular pulse (Λ), in 9 harmonics, with a centre at μ_i and a period of $\frac{2\pi}{16}$. In this way, each 'off-centre' 2nd harmonic hot-streak peak (that is, hot-streak peaks located at the values of $\theta \neq \frac{n2\pi}{16}$) are contributed to equally by its two adjacent burners and when all burners are active the second wave is approximately a unit distribution at all values of θ. The triangular pulse is implemented as a 9 term Fourier series in order to ensure smoothness (something which is not a property of a true triangular pulse) whilst also keeping the contribution of the triangular pulse wave to the 32EO component of the final temperature distortion below 0.1%, for the case where all burners are active. The final equation for the contribution of the second harmonic of the temperature distortion is then given by Eqn (3), and is an accurate representation of the 2nd harmonic content of the original scaled distortion to within $0.5K$ at all radii, for the all burners active case. A visual comparison of the resultant hot-streaks can be seen in Fig 2.

2.4 Burner Cases and Simulation Procedure

This paper considers 5 cases with different temperature distortion configurations. The case names and burner can on-off information is laid out in Table 2.4. 'NB', has no hot-streaks imposed at the inlet and is the same case used for the validation in Fig 3. The other cases are defined as 'BB' (blocked burner) followed by the configuration of the failed burners. The case BB-0 NP has all burners active, but with 'no parameterisation' of the inlet temperature distortion. Due to a desire to investigate the causes of forcing, rather than the effects, this paper evaluates measurements of rotor blade unsteady pressure, rather than attempting to relate this information to blade vibration amplitudes. In this way, the results are more general and can be applied more readily to any turbine blade. All unsteady pressure measurements have been normalised by the absolute inlet dynamic pressure ($\frac{1}{2}\rho c_1^2$).

Case	NB	BB-0 NP	BB-0	BB-1	BB-1-9
Burners On (i)	-	$1-16$	$1-16$	$2-16$	$2-8,10-16$
Burners Off	-	-	-	1	1,9

TABLE 1. CASE CODES AND THEIR CONFIGURATION OF ON-OFF BURNERS

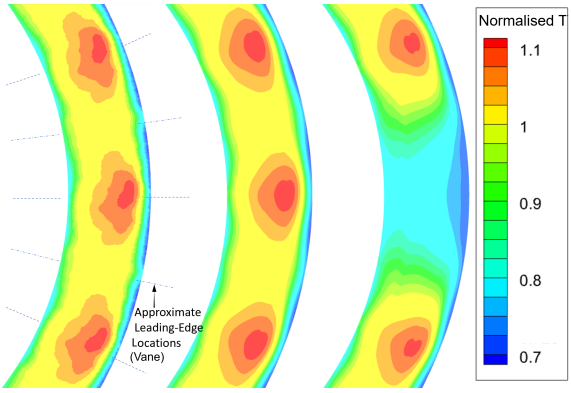

FIGURE 2. STATIC TEMPERATURE CONTOURS OF INLET DISTORTIONS FOR THE SCALED ENGINE DATA, PARAMETERISED EQUIVALENT AND 1 BURNER FAILED CASES, NORMALISED *WRT* T_{01}

Quantity	Experiment	Simulation	% Difference
P_{01} (bar)	$4.6^{+}_{-}2\%$	4.600	0.00
T_{01} (K)	$444^{+}_{-}2\%$	443.9	−0.02
$M_{h2,isen}$	$1.034^{+}_{-}2\%$	1.041	0.64
$M_{c2,isen}$	$0.925^{+}_{-}2\%$	0.8976	−2.96
Ω (rpm)	$9500^{+}_{-}2\%$	9500	0.00
P_{h3} (bar)	$1.428^{+}_{-}2\%$	1.453	1.76
P_{c3} (bar)	$1.435^{+}_{-}2\%$	1.472	2.61

TABLE 2. OPERATING POINT ANALYSIS: EXPERIMENT VS SIMULATION, DATA FROM [17]

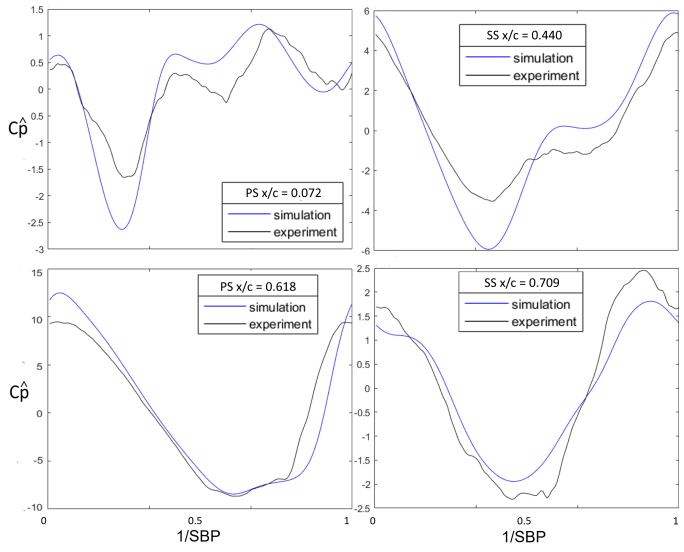

FIGURE 3. TIME HISTORIES OF UNSTEADY PRESSURE COEFFICIENT AT VARIOUS BLADE LOCATIONS FOR 1 SBP

3 VALIDATION OF MODELLING SET-UP

The steady state operating point is set to match that of [17], with a comparison of the achieved match given in Table 2. All parameters are within the $^{+}_{-}2\%$ tolerance except for $M_{c2,isen}$ and P_{c3}, which indicate that the fluid velocities at the casing may be slightly under-predicted. However, this error is small. In addition to this, the results of comparisons of unsteady pressure coefficient at 4 pressure tap locations (pressure side $x_c = 0.072$, suction side $x_c = 0.44$, pressure side $x_c = 0.618$, suction side $x_c = 0.709$) against equivalent points on the simulated blade surface can be seen in Fig 3. Unsteady pressure is a measurement of pertubations of static pressure about the mean pressure on the blade surface. The unsteady pressure coefficient is defined in Eqn 4. Unsteady pressures are the primary metric through which this work has been evaluated and results demonstrate that the described numerical set-up is able to capture accurately the unsteady behaviour.

$$C_{\hat{p}} = \frac{p - \overline{p}}{\frac{1}{2}\rho c_1^2} \tag{4}$$

3.1 Effect of Burner Cans on Operating Point

Before looking at the unsteady pressure brought about due to the hot-streaks, it is worth ensuring the operating point of the MT1 stage has not drastically changed. The introduction of hot-streaks into the MT1 rig has negligible impact on the time averaged performance metrics, outlined in Table 3. There is a small rise in the losses from the passage of about 0.1% when measured using total pressure loss coefficient, Y_p. This is expected to be within the rotor passage, given previous work highlighting the effect hot-streaks have within the rotor compared to the stator [3][24]. There is a small difference in the rotor blade pressure distribution at midspan, shown in Fig 4, which are consistent with higher blade loading, but this difference is considered minor. The other change brought about through the introduction of the hot-streak is a radial distribution of temperature, uniformly distributed in the case 'NB', which persists across the vane. However, as can be seen from the reaction, this does not lead to a larger than expected static enthalpy drop across the vane.

Quantity	NB	BB-0 NP	BB-0	BB-1	BB-1-9
$T_{01}/T_{01,NB}$	1.000	1.000	1.000	0.973	0.948
Reaction	0.443	0.443	0.442	0.446	0.450
Capacity $(\frac{kg\sqrt{K}}{Pa}e^{-4})$	7.824	7.830	7.833	7.833	7.832
$Y_p(\%)$	6.11	6.28	6.26	6.25	6.35

TABLE 3. TIME AVERAGED NORMALISED QUANTITIES FOR THE NB, BB-0 NP, BB-0, BB-1, BB-1-9 CASES

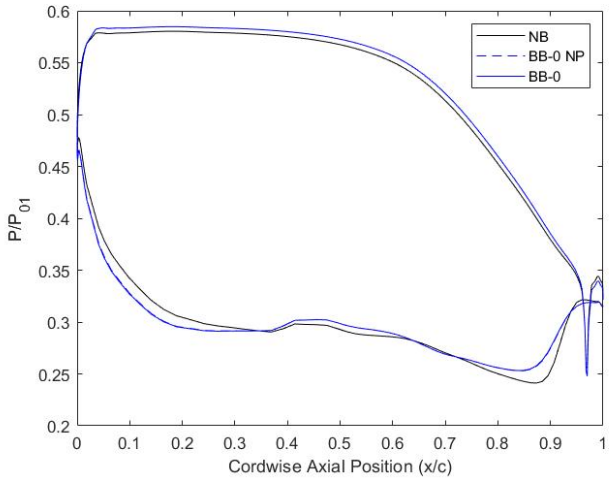

FIGURE 4. MEAN PRESSURE PROFILE FOR CASES RUN AT THE MT1 OPERATING POINT (NB,BB-0 NP,BB-0)

4 ANALYSIS OF UNSTEADY FORCING

4.1 Hot-Streak Induced Forcing

The first case investigated is the forcing caused by the hot-streaks. The 16EO unsteady pressure magnitude contours across the rotor blade pressure and suction sides can be seen in Fig 5. The main driver of this unsteadiness is the localised T rise across the central portion of the passage, leading to an increase in absolute circumferential velocity $c_{\theta 2}$ and, therefore, stage loading coefficient ψ. This effect was first reported by [24] and can be demonstrated through measurements taken of the 16^{th} circumferential mode component of these quantities at the vane exit, shown in Fig 6*a* and 6*b* below. For simplicity the term 16EO will be used to describe these variations due to their exciting 16EO unsteadiness in the rotor. The pressure side contours are dominated by this effect, as is the green zone in the centre of the suction side surface immediately before the throat, both marked with point 4

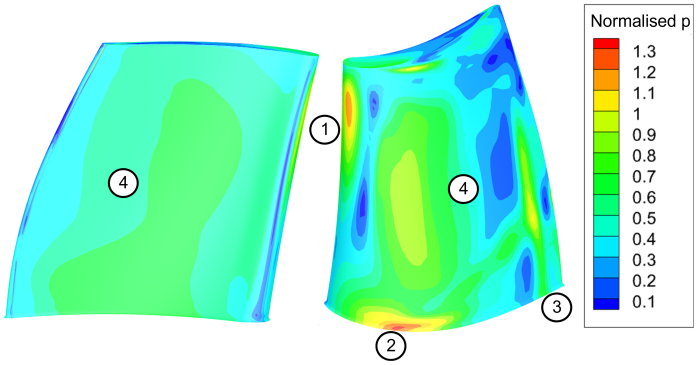

FIGURE 5. UNSTEADY PRESSURE MAGNITUDE CONTOURS ACROSS ROTOR PRESSURE (LEFT) AND SUCTION (RIGHT) SIDES AT EO16, FOR CASE BB-0. NORMALISED *WRT* STAGE INLET DYNAMIC PRESSURE

in Fig 5. This potential effect, which acts across the majority of the blade span, is the greatest contributor to forcing.

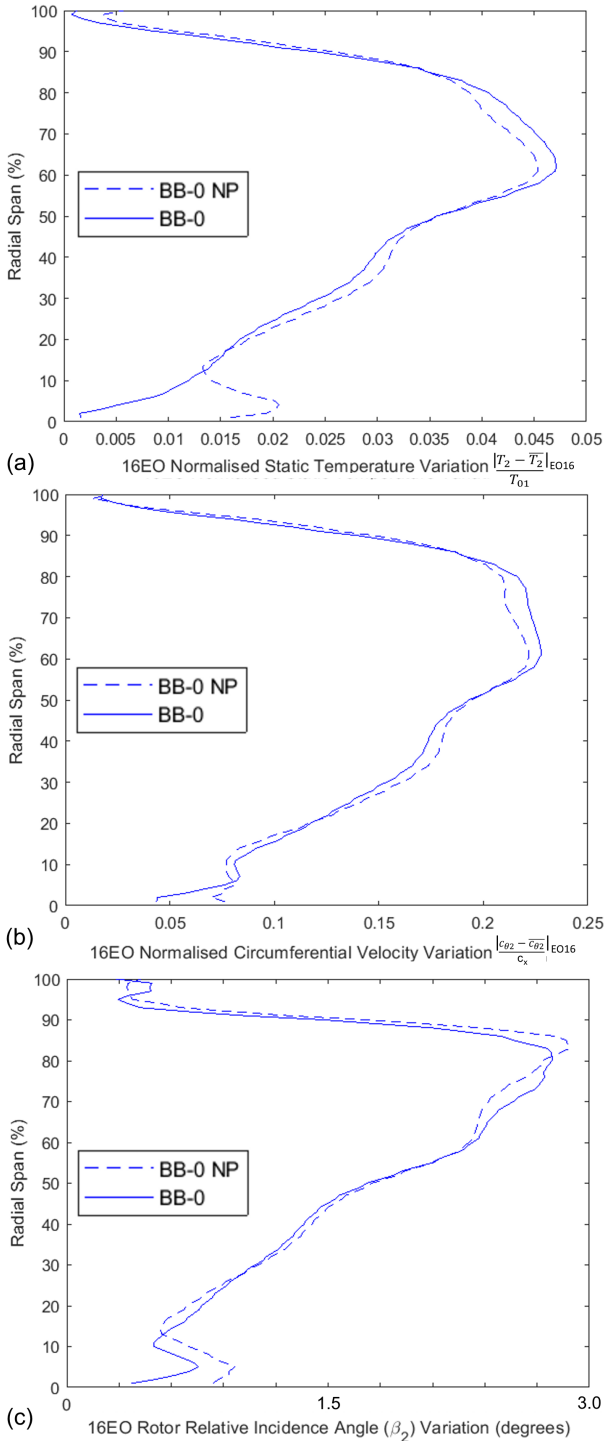

FIGURE 6. RADIAL DISTRIBUTIONS OF 16EO CIRCUMFERENTIAL VARIATIONS IN T_2,$c_{\theta 2}$ AND β_2, FOR THE BB-0 AND BB-0 NP CASES, NORMALISED WHERE NOTED.

Besides the blade working harder due to this increase in ψ, there are three large unsteady pressure spikes on the blade suction side, attributable to a combination of potential and viscous phenomena (labelled 1 to 3 in Fig 5). The unsteady pressure peak at point 1 is attributed to the hot-streak at this location interfering with the vane wake 'negative-jet' [25], leading to an increase in absolute velocity within the jet and, therefore, rotor relative flow angle. The radial distribution of burner can frequency unsteadiness in β_2 can be seen in Fig 6*c* and shows a 2.7° variation in the parameter at $82.5\%b_h$, for the BB-0 case. It is interesting that the radial distribution of β_2 unsteadiness shown in Fig 6, mirrors closely the inlet 16EO unsteadiness in T_1 (shown in Fig 7) which has its peak at $79\%b_h$, rather than the radial distribution of T_2, which is the driver of $c_{\theta 2}$.

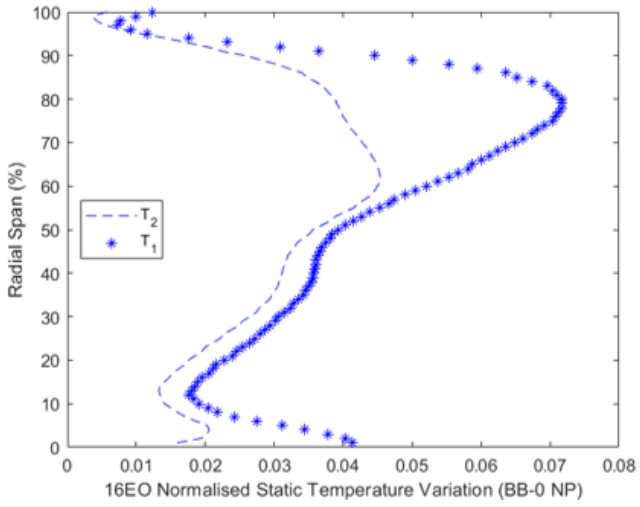

FIGURE 7. COMPARISON OF THE 16EO CIRCUMFERENTIAL VARIATION IN T ACROSS ALL RADII AT VANE INLET AND OUTLET, NORMALISED *WRT* T_{01}

The large unsteady pressure amplitude at point 2 in Fig 5 is attributable to an interference of the hot-streak with the vortices at the hub. Hot-streaks in the rotor row are well known drivers of increased secondary vorticity [3]. An increase in $c_{\theta 2}$, caused by the hot-streak, and the associated increase in p difference across the passage increases the streamwise vorticity introduced to the boundary layer by the row, the size of the end wall cross-flow and the speed at which the pressure-leg horseshoe vortex (PLH) is pulled from the pressure side to the suction side of the adjacent blade. Fig 8 tracks the progression of the principle hub vortices, in two different passages (the hot streak effected passage (A) and a cooler passage (B)) across three axial cuts (1, 2 and 3) spanning the the first half of the unsteady pressure feature. It is clear from the figure that this feature is occurring at the point the PLH is arriving at the blade suction side, with the vortex arriving sooner in the case of the hotter passage, (A). In keeping with results published in [26], the hot-streak also pulls the passage vortex toward the blade midspan, a phenomenon which can be seen in the un-

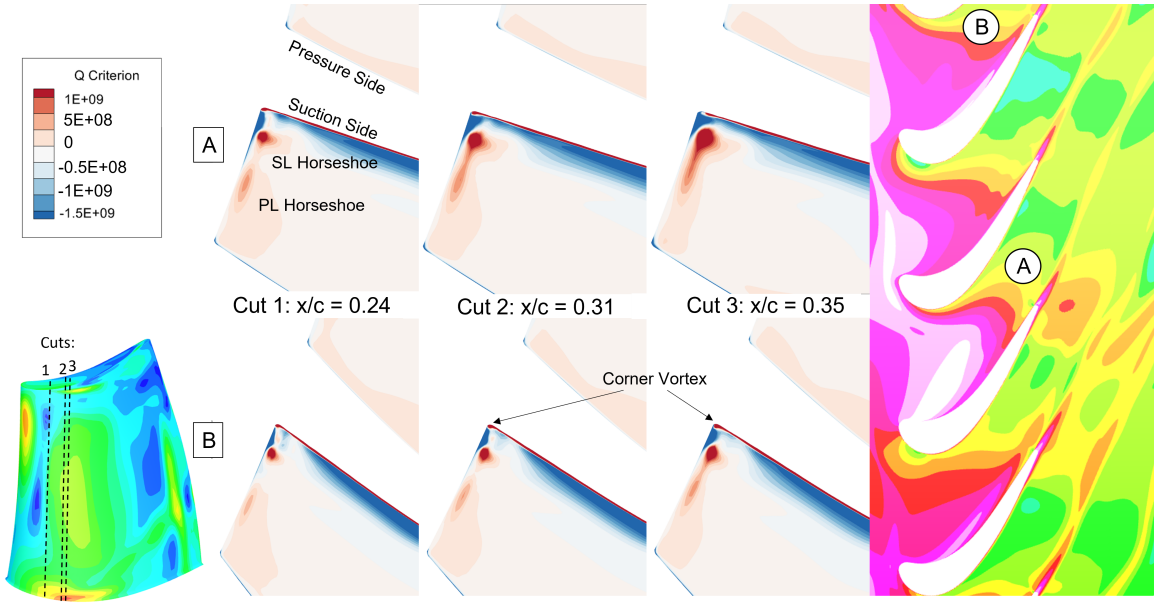

FIGURE 8. MIGRATION OF VORTICES: AXIAL CUTS (LOCATIONS OF WHICH ARE IDENTIFIED BY CHORDWISE POSITION (X/C) AND LOCATION RELATIVE TO THE ROTOR BLADE UNSTEADY PRESSURES (BOTTOM-LEFT)) THROUGH 2 ROTOR PASSAGES (A (ABOVE) AND B (BELOW) ON THE MIDSPAN TEMPERATURE CONTOUR (RIGHT)) OF Q-CRITERION

steady pressure contours of Fig 5, through the green trail of high unsteady pressure leading from point 2 to the spanwise patch labelled point 3. What is taking place here is a forced convection effect where the cold fluid of the vortex is moving toward the area occupied by the low ρ hot-streak fluid. This is the process which drives the much reported result of hot streaks migrating to the blade pressure side and spreading out [27]. The speed and location of this migration are not noticeably effected at the 16EO by variations in T, but it is likely that the added vorticity and increased end wall cross flow brought about by the hot-streak means that by the time the PLH emerges as the passage vortex, it is considerably stronger due to the effect of the hot-streak.

The unsteady pressure feature at point 3 is caused by the movement and intensity change of a shock which is occurring immediately downstream of the passage section. The shock moves aftward in the absence of the hot-streak from the trailing edge of the passage. This effect is most clearly visible for the failure cases and will be described when discussing burner failures below. Finally, the hot-streak interferes little with the tip vortex, however, the greater pressure difference between rotor suction and pressure side, brought about through oscillations in ψ, leads to a small unsteadiness at the 16EO frequency in the blade tip region. However, this unsteady pressure is neither great enough, nor acting across a large enough area to cause a significant effect on total blade forcing.

Before going any further, it is worth briefly discussing the SBPF forcing. By definition, the SBPF is a HEO unsteadiness, so for this reason our interest in it extends only to determining its relative magnitude and its variation under the influence of a hot-streak. The 16EO unsteadiness is roughly $\frac{1}{6}$ of the magnitude of the 32EO (SBPF) unsteadiness, measured in terms of unsteady lift force, for the all burners active case. This difference is due to the hot-streak temperature intensity ratio ($\frac{T_{max}}{T_{mean}}$) being reduced during scaling to ensure hot-streak shape was maintained. As such, the introduction of hot-streaks has almost negligible effect on the 32EO forcing.

4.2 Effect of Inlet Distortion Parameterisation

As explained in Section 2.3, in order to begin the process of simulating burner failure, the inlet distortion had to be parameterised so that it could be represented as a sum of 16 discrete temperature sources. The differences between the parameterised and original distortion are very minor, with any noticeable differences occuring in the 3*rd* spatial harmonic of temperature (48EO) or higher.

The bulk averaged aerodynamic properties for both unsteady runs can be seen in Table 3 and show very little difference (BB-0 AND BB-0 NP lines). This is echoed by the rotor pressure profile shown in Fig 4 and although not shown, the radial distributions of circumferentially averaged properties are, also, all identical.

There are, however, noticeable (albeit minor) differences in the vane exit radial distributions of 16EO unsteady quantities, shown in Fig 6. One such difference is that the parameterised hot-streak stays slightly more concentrated toward the hot-streak centre, with less heat dispersed across the row. Considering the main forcing mechanism laid out above, it will not be surprising to find that this leads to a difference in forcing. BB-0 NP has a 16EO unsteady lift force (defined in Eqn 5) equal to 80% of its parameterised equivalent, this is despite a number of other effects pulling in the opposite direction. In fact, the passage vortex

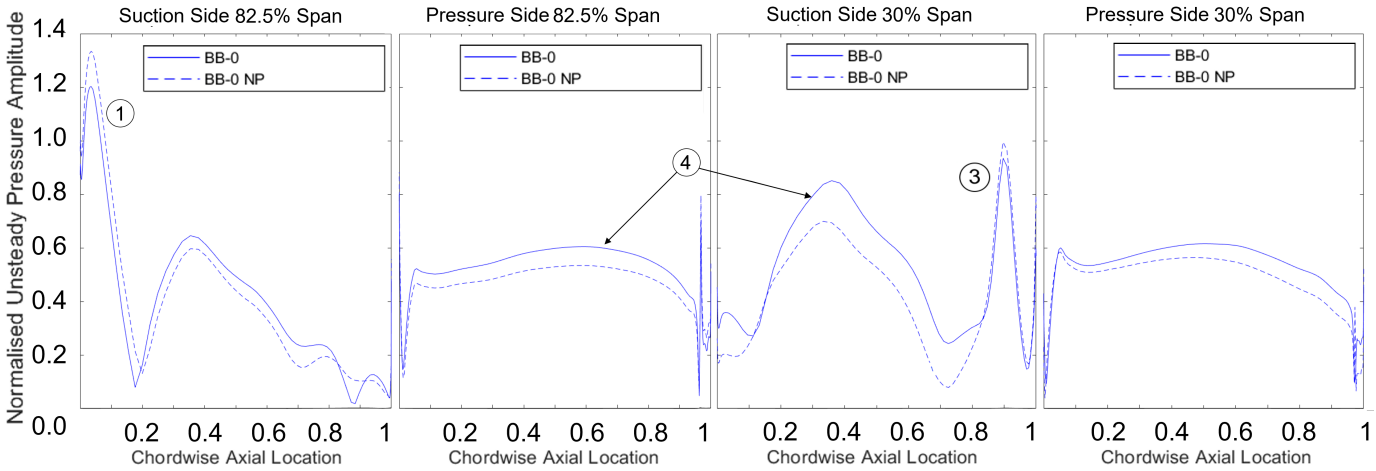

FIGURE 9. NORMALISED UNSTEADY PRESSURE MAGNITUDES AT EO16, ROTOR SUCTION/ PRESSURE SIDES AT 82.5% AND 30%b_h

unsteadiness, shock unsteadiness and wake negative-jet unsteadiness are all higher for the BB-0 NP case. The passage vortex unsteady pressure spike is affected by a visible temperature spike between $0-5\%b_h$ for the BB-0 NP, shown in Fig 6*a*. This is not present for the BB-0 case, and has its origin in the inlet distortion hub wall region. A higher β_2 variation toward the casing, visible in Fig 6*b*, leads to a higher unsteady pressure magnitude in this region as well.

Fig 9 shows radial cuts of the same unsteady pressure magnitudes shown in Fig 5, at $30\%b_h$ and $82.5\%b_h$, for both the BB-0 and BB-0 NP cases. Illustrated clearly is the higher unsteady pressures across the BB-0 rotor blade, except for in the isolated areas where peaks are seen on the suction side, such as for the negative-jet and shock related pressure events. The low relative unsteady lift, based solely on the reduction in the $c_{\theta 2}$ forcing mechanism, highlights the importance of that forcing mechanism in comparison to the others.

It is worth briefly touching on this seemingly large unsteady lift force discrepency caused by the hot-streak parameterisation. The main differences in forcing coming from a distortion at the hub wall (outside the representable region) and through some effect due to the presence of higher order spatial harmonics of temperature. However, all of the relevant features from the BB-0 NP cases are still present with the right relative phases and in the right locations, both radially and axially, meaning the forcing mechanisms can be easily identified and corroborated for the BB-0 case.

Burner Failure Induced Forcing

In order to first assess the relative significance of the burner failures, Fig 10 shows a comparison of the unsteady lift force at every LEO for the BB-0, BB-1 and BB-1-9 cases. Unsteady lift force is an integral over the entire blade surface of the pressure normal to the surface dot product with the lift modeshape m_L, which is defined normal to c_2 (see Eqn 5). It is akin to a modal force, only without the specific mode with which the

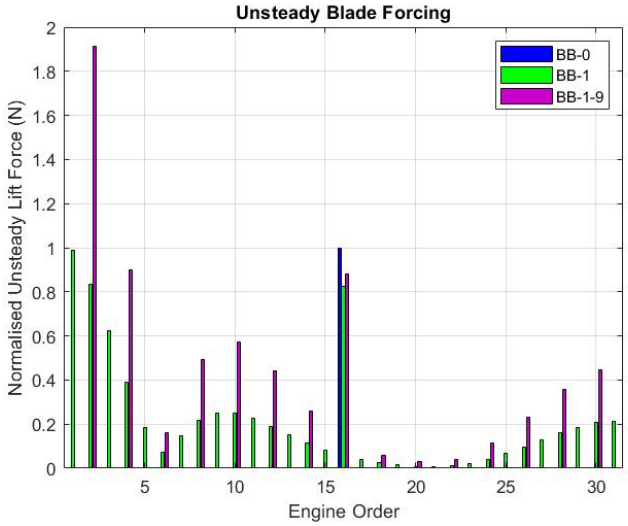

FIGURE 10. UNSTEADY LIFT FORCE ACROSS ALL LEOS, COMPARISON OF BB-0, BB-1 & BB-1-9. NORMALISED *WRT* THE UNSTEADY LIFT FOR BB-0, EO16

blade vibrates, and gives an integrated way of assessing the total unsteady pressure seen by the blade at a particular engine order.

$$F_L = \int p(x,y,z,t)\vec{n} \cdot \vec{m_L} dA \tag{5}$$

As can be seen in Fig 10, the 2EO forcing caused by the symmetric burner failed event BB-1-9 is almost twice the magnitude of the unsteady lift seen at the 16EO due to the BB-0 case. The primary reason for this difference, is that the circumferential variation in temperature caused by a burner failure is far larger than that caused by a non-uniformity of combustion brought about by a burner system. Fig 11 displays this information through radial distributions of circumferential variation

in T_2 and β_2 for all three parameterised cases in terms of their principle (lowest EO) disturbance. The relative distortions in β_2, in particular, mirror the equivalent unsteady lift forces on Fig 10 extremely well. Furthermore, the 2EO forcing in BB-1-9 is significantly higher than the 1EO forcing in BB-1. This is to be expected, as the BB-1-9 distortion is concentrated on fewer EOs (even harmonics only), the 2EO temperature distortion from BB-1-9 is twice as great as the 1EO distortion in BB-1. There are also a number of higher harmonics and Tyler-Sofrin modes excited by both burner failure arrangements, of which the 4EO forcing for the BB-1-9, exhibits a significant normalised unsteady lift of 0.9. Analysis of the forcing mechanisms associated with the Tyler-Sofrin modes will not be conducted in this paper, although, it should be noted that significant excitations at multiple EOs pose a key challenge to designing turbines for forcing attenuation.

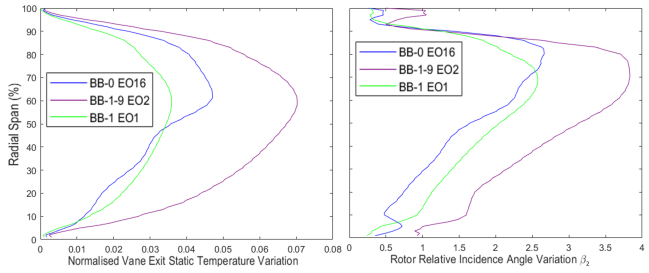

FIGURE 11. RADIAL DISTRIBUTION COMPARISON OF THE 16EO (BB-0), 2EO (BB-1-9) AND 1EO (BB-1) CIRCUMFERENTIAL VARIATION IN T_2 AND β_2. T_2 NORMALISED *WRT* T_{01}.

The contours of unsteady pressure at the 2EO for the BB-1-9 case are shown in Fig 12, whilst a relative Mach contour and midspan pressure distribution comparison for a cold streak effected rotor blade can be seen in Fig 13 and Fig 14. The main forcing mechanism is the change in relative flow angle β_2. This is not thought to be connected to the vane wake, as it was for the 16EO hot-streak forcing, but brought about by the change in $c_{\theta 2}$: itself a result of the T_2 variation. The radial distribution of 2EO unsteadiness in these quantities can be seen in Fig 11. β_2 has a maximum at 70%b_h (of 3.84°) in this case and stays high at a greater range of radii than the effect seen due to the wake interference. The result of this change is to move the stagnation point onto the suction side. There are two effects of this. Firstly, the fluid acceleration on the suction side is more gradual (see Fig 14). This is the effect causing the large unsteady pressure zone on Fig 12 and the lack of a high relative Mach number zone at the leading edge of Fig 13, marked point 1 on each figure. Secondly, due to the thick leading edge of the turbine geometry, fluid is able to accelerate around the leading edge and onto the pressure side without separating. This causes a low pressure dip at the pressure side leading edge, seen on the 'Cold-streak Blade' of Fig 14, and this is causing the unsteady pressure at the same location on Fig 12, marked point 2 on each figure. There is also unsteadiness in the trailing edge shock region, with the shock location mov-

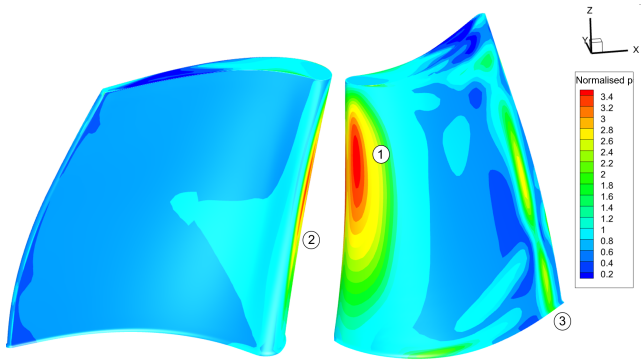

FIGURE 12. UNSTEADY PRESSURE MAGNITUDE CONTOURS ACROSS ROTOR PRESSURE (LEFT) AND SUCTION (RIGHT) SIDES AT EO2, FOR BB-1-9 CASE. NORMALISED *WRT* STAGE INLET DYNAMIC PRESSURE

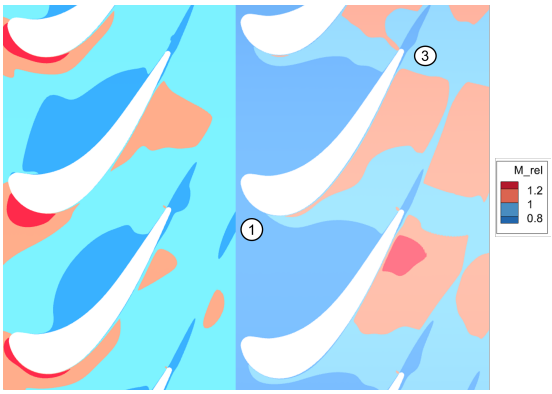

FIGURE 13. CONTOURS OF RELATIVE MACH NUMBER AT 0.4%b_h, FOR NB (LEFT) AND BB-1-9 COLD STREAK AFFECTED CASE (RIGHT)

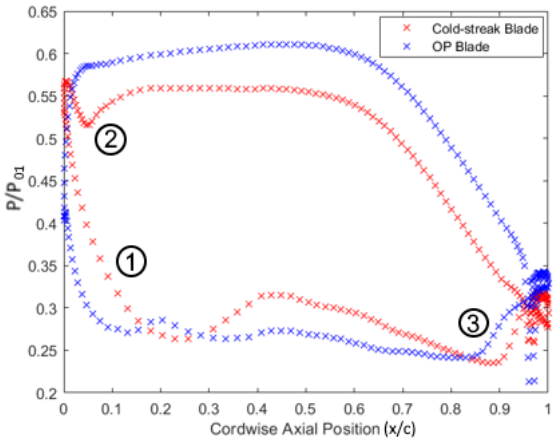

FIGURE 14. NORMALISED PRESSURE ACROSS MIDSPAN FOR ROTOR BLADE UNDER THE INFLUENCE OF A COLD STREAK AND A PERIODICALLY SIMILAR BLADE AT THE NORMAL OPERATING POINT (OP), BOTH FROM BB-1-9

ing aftward under the influence of a cold-streak, a phenomenon shown clearly at point 3 in Figs 13 and 14. This is caused by a variation in blade exit flow angle, β_3 which varies across the outlet metal angle (by as much as 4.6° in the case BB-1-9), changing the location of the point of minimum effective passage width and, hence, the shockwave location. There are several possible causes of this. β_3 will be influenced by the change in incidence β_2, shown in Fig 11, as well as through a change in $c_{\theta,rel}$ due to temperature variations in the rotor row.

The final potentially significant result is the remarkable similarity in rotor blade unsteady pressure contours between the 1EO on case BB-1 and the 2EO in case BB-1-9, shown in Figs 15 and 12. Both show the exact same forcing mechanisms acting on the blade in the same locations, with the same relative magnitudes, only the unsteady pressure magnitudes in the BB-1 case are significantly lower for the reasons laid out above.

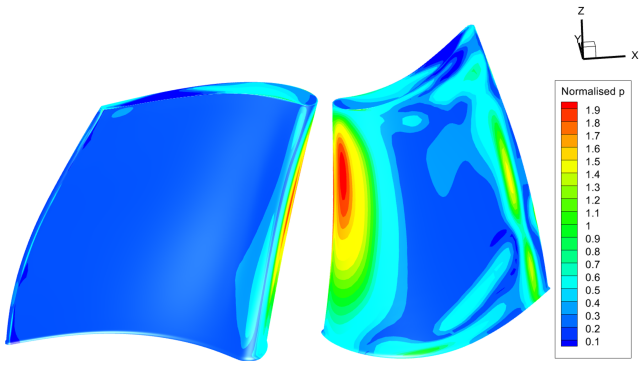

FIGURE 15. UNSTEADY PRESSURE MAGNITUDE CONTOURS ACROSS ROTOR PRESSURE (LEFT) AND SUCTION (RIGHT) SIDES AT EO1, FOR BB-1 CASE. NORMALISED *WRT* STAGE INLET DYNAMIC PRESSURE

5 CONCLUSIONS

This paper carried out a computational parametric study of LEO forced response in a benchmark turbine rig, under the influence of hot-streaks and burner failed events. With reference to the objectives set out in Section 1, the following can be concluded:

At the hot-streak frequency, the primary driver of unsteady pressure is a oscillation in stage loading factor, ψ caused by a change in $c_{\theta 2}$, itself a result of a T_2 variation. In addition to this, there is a vane wake interaction and a shock interaction with the hot-streak. An interaction with the hub vortices, which is a less significant driver of unsteady pressure, is also present. However, the extent to which this interaction is an important driver of LEO forced response is questionable. Unsteady pressures at a blade root are unlikely to cause significant vibration in low frequency mode shapes, where LEO resonance is expected to occur. In real engine turbine geometries there is also, often, a bleeding of the hub wall boundary layer through cavities upstream of the blade, which would reduce the strength of the passage vortex. There was almost negligible interaction between the hot-streak and the tip vortex.

The dominant drivers of forcing in the case of a burner failure is still the change in $c_{\theta 2}$, only it is felt as a change in relative incidence angle β_2, localised at the leading edge. The unsteadiness in the shock position and intensity are also more significant for the burner failed cases. All of the forcing mechanisms seen due to the presence of a hot-streak can also be seen due to their absence in the burner failed cases.

The extent to which burner failure can drive forced response, as measured through modal force, is highly dependent on the temperature of the distortion. This research found a linear relationship between the principle vane exit temperature distortion magnitude and the unsteady lift force at the corresponding EO. As such it is not possible with these low temperature simulations to assess the magnitude of LEO hot-streak forcing in relation to the HEO SBP forcing for a real engine. The symmetric burner failed event proved to be approximately twice the forcer of the burner can hot-streak itself, when measured using unsteady lift force. How severe this is for blade vibration amplitudes will depend on the natural frequencies of the specific blade of interest, but the location of the unsteady pressure peaks, at the leading and trailing edge, would likely produce high modal forces for vibration modes susceptible to unsteady pressure in these areas, such as 1*st* torsion. The burner failure configuration proved to be a crucial determinant of unsteady pressure magnitudes, with the symmetric burner failed event, being spread over less engine orders, proving a more significant source of forcing at the engine orders for which it was present.

In terms of other temperature distortion parameters that will effect the severity of hot-streaks, it is speculated that the clocking position is likely to be extremely important. The hot streaks are clocked so as to take advantage of 'phantom cooling', an effect that will result in a higher than otherwise drop in T across the vane, illustrated in Fig 7. Given the relative importance of the $c_{\theta 2}$ forcing mechanism, this will likely have reduced the forcing seen due to the hot-streaks. The effort taken to accurately capture the hot-streak shape, has proved the novel step that has allowed the tracking of the forcing mechanisms carried out in this paper. Through the differences in results for the parameterised burner case and the non-parameterised equivalent, it is clear that the presence of higher spatial harmonic components of the hot-streak has an effect on the attenuation of the hot-streak across the vane.

ACKNOWLEDGMENT

The authors would like to acknowledge the contribution from colleagues at Rolls-Royce plc, namely Davendu Kulkarni, Bharat Lad, Richard Setchfield and Adrian Jones, for work and support to facilitate this research.

Data Access Statement

Data supporting this study cannot be made available due to commercial confidentiality agreements.

Open Access Statement

REFERENCES

[1] Vahdati, M., Sayma, A. I., and Imregun, M., 2000. "An integrated nonlinear approach for turbomachinery forced response prediction. part ii: case studies". *Journal of Fluids and Structures,* ***14***(1), pp. 103–125.

[2] Sayma, A., Vahdati, M., and Imregun, M., 2000. "Turbine forced response prediction using an integrated non-linear analysis". *Proceedings of the Institution of Mechanical Engineers, Part K: Journal of Multi-body Dynamics,* ***214***(1), pp. 45–60.

[3] Lakshminarayana, B., 1975. "Effects of inlet temperature gradients on turbomachinery performance". *Journal of Engineering for Gas Turbines and Power,* ***97***(1).

[4] Denton, J. D., 1993. *Loss mechanisms in turbomachines*, Vol. 78897. American Society of Mechanical Engineers.

[5] Jöcker, M., Kessar, A., Fransson, T. H., Kahl, G., and Rehder, H.-J., 2006. "Comparison of models to predict low engine order excitation in a high pressure turbine stage". In *Unsteady Aerodynamics, Aeroacoustics and Aeroelasticity of Turbomachines*. Springer, pp. 145–159.

[6] Elliot, R., Sayma, A., and Imregun, M., 2005. Aeromechanical design of damped high pressure turbine blades subject to low engine order forcing. Tech. rep., Rolls-Royce LTD Derby (UK).

[7] Manwaring, S. R., and Kirkeng, K. L., 1998. "Forced response vibrations of a low pressure turbine due to circumferential temperature distortions". In *Unsteady Aerodynamics and Aeroelasticity of Turbomachines*. Springer, pp. 379–392.

[8] Ioannou, E., 2015. "The effects of temperature distortion on aerodynamics and low engine order forced response in axial turbines". PhD thesis, City University London.

[9] Mayorca, M. A., Bladh, R., and Ozturk, U., 2013. "Estimation of burner can-induced excitation levels in an industrial gas turbine". In Turbo Expo: Power for Land, Sea, and Air, Vol. 55270, American Society of Mechanical Engineers, p. V07BT33A013.

[10] Mayorca, M. A., Torres, A., Kharyton, V., and Bladh, R., 2015. "Estimation of burner-can induced excitation response of an industrial low pressure turbine blade: Validation against prototype test data". In Turbo Expo: Power for Land, Sea, and Air, Vol. 56772, American Society of Mechanical Engineers, p. V07BT34A010.

[11] Fridh, J., Laumert, B., and Fransson, T., 2012. "Forced response in axial turbines under the influence of partial admission". In Turbo Expo: Power for Land, Sea, and Air, Vol. 44731, American Society of Mechanical Engineers, pp. 1419–1429.

[12] Tyler, J., and Sofrin, T., 1962. "Axial flow compressor noise studies". *SAE Trans*, pp. 309–332.

[13] Terstegen, M., Sanders, C., Jeschke, P., and Schoenenborn, H., 2019. "Rotor–stator interactions in a 2.5-stage axial compressor—part i: Experimental analysis of tyler–sofrin modes". *Journal of Turbomachinery,* ***141***(10).

[14] Bréard, C., Green, J., and Imregun, M., 2003. "Low-engine-order excitation mechanisms in axial-flow turbomachinery". *Journal of Propulsion and Power,* ***19***(4), pp. 704–712.

[15] Kafedzhiyski, N., and Mayorca, M., 2021. "Practical method for burner staging turbine forced response evaluation". In Turbo Expo: Power for Land, Sea, and Air, Vol. 85024, American Society of Mechanical Engineers, p. V09AT23A008.

[16] Sureshkumar, P., Lee, K.-B., Puente, R., and Stapelfeldt, S., 2022. "Impact of the spatial arrangement of inlet distortions on resonant fan response". In Proceedings of Global Power and Propulsion Society.

[17] Hilditch, M., Smith, G., Anderson, S., Chana, K., Jones, T., Ainsworth, R., and Oldfield, M., 1996. "Unsteady measurements in an axial flow turbine". In AGARD CONFERENCE PROCEEDINGS AGARD CP, AGARD, pp. 24–24.

[18] Sayma, A. I., Vahdati, M., and Imregun, M., 2000. "An integrated nonlinear approach for turbomachinery forced response prediction. part i: formulation". *Journal of Fluids and Structures,* ***14***(1), pp. 87–101.

[19] Jorgenson, P., and Turkel, E., 1993. "Central difference tvd schemes for time dependent and steady state problems". *Journal of Computational Physics,* ***107***(2), pp. 297–308.

[20] Lee, K.-B., Wilson, M., and Vahdati, M., 2018. "Validation of a Numerical Model for Predicting Stalled Flows in a Low-Speed Fan—Part I: Modification of Spalart–Allmaras Turbulence Model". *Journal of Turbomachinery,* ***140***(5), 04. 051008.

[21] Milli, A., and Shahpar, S., 2012. "Padram: Parametric design and rapid meshing system for complex turbomachinery configurations". In Turbo Expo: Power for Land, Sea, and Air, Vol. 44748, American Society of Mechanical Engineers, pp. 2135–2148.

[22] Simonassi, L., Zenz, M., Bruckner, P., Pramstrahler, S., Heitmeir, F., and Marn, A., 2021. "Aerodynamic and aeroelastic experimental investigation on the propagation of inlet temperature distortions in a low pressure turbine stage". In Proceeding of 14th European Conference of Turbomachinery, Fluid Dynamics, and Thermodynamics ETC14, April 12-16, 2021, virtual.

[23] Gauss, C. F., 1823. *Theoria combinationis observationum erroribus minimis obnoxiae*, Vol. 2. H. Dieterich.

[24] Beard, P. F., Smith, A., and Povey, T., 2011. "Impact of severe temperature distortion on turbine efficiency". In Turbo Expo: Power for Land, Sea, and Air, Vol. 54679, pp. 681–694.

[25] Salvadori, S., Montomoli, F., Martelli, F., Adami, P., Chana, K., and Castillon, L., 2011. "Aerothermal study of the unsteady flow field in a transonic gas turbine with inlet temperature distortions". *Journal of Turbomachinery,* ***133***(3).

[26] Gaetani, P., Persico, G., Pinelli, L., Marconcini, M., and Pacciani, R., 2020. "Computational and experimental study of hot streak transport within the first stage of a gas turbine". *Journal of Turbomachinery,* ***142***(8).

[27] Dorney, D. J., Gundy-Burlet, K. L., and Sondak, D. L., 1999. "A survey of hot streak experiments and simulations". *International Journal of Turbo and Jet Engines,* ***16***(1), pp. 1–16.